Available online at www.sciencedirect.com
SCIENCE DIRECT®
Journal of Magnetic Resonance 168 (2004) 164–174
JMR Journal of Magnetic Resonance
www.elsevier.com/locate/jmr

Distortion-free single point imaging of multi-layered composite sandwich panel structures

Andrew E. Marble,[a,b] Igor V. Mastikhin,[a] Rod P. MacGregor,[a] Mohamad Akl,[a,b] Gabriel LaPlante,[a,c] Bruce G. Colpitts,[b] Pearl Lee-Sullivan,[c] and Bruce J. Balcom[a,*]

[a] *MRI Centre, Department of Physics, P.O. Box 4400, University of New Brunswick, Fredericton, New Brunswick, Canada E3B 5A3*
[b] *Department of Electrical and Computer Engineering, P.O. Box 4400, University of New Brunswick, Fredericton, New Brunswick, Canada E3B 5A3*
[c] *Department of Mechanical Engineering, P.O. Box 4400, University of New Brunswick, Fredericton, New Brunswick, Canada E3B 5A3*

Received 4 December 2003; revised 10 February 2004

Abstract

The results of a magnetic resonance imaging (MRI) investigation concerning the effects of an aluminum honeycomb sandwich panel on the B_1 and B_0 fields and on subsequent image quality are presented. Although the sandwich panel structure, representative of an aircraft composite material, distorts B_0 and attenuates B_1, distortion-free imaging is possible using single point (constant time) imaging techniques. A new expression is derived for the error caused by gradient field distortion due to the heterogeneous magnetic susceptibility within a sample and this error is shown not to cause geometric distortion in the image. The origin of the B_0 distortion in the sample under investigation was also examined. The graphite-epoxy 'skin' of the panel is the principal source of the B_0 distortion. Successful imaging of these structures sets the stage for the development of methods for detecting moisture ingress and degradation within composite sandwich structures.

Keywords: Inhomogeneous susceptibility; MRI; Sandwich panels; Composites; SPRITE

1. Introduction

Sandwich panel constructions with honeycomb cores are widely used in structural aerospace applications such as aircraft flight control surfaces and stabilizers [1]. In general, these sandwich panels are made by bonding graphite reinforced epoxy skins to an aluminum honeycomb core using a thin layer of epoxy adhesive [1]. A cut-away diagram illustrating this construction can be seen in Fig. 1. Sandwich structures are considered high performance materials because of their high stiffness to weight ratio. However, the structural integrity of the panel depends on the adhesive layer. It has been observed that epoxy adhesives tend to degrade when in contact with water, a condition that can exist inside of sandwich panels in some aerospace applications [2]. Water ingress into aircraft flight control surfaces has been linked to in-flight failure in some aircraft [3].

There is an ongoing effort to develop a nondestructive technique to detect anomalies within sandwich structures before failure, and many different approaches have been investigated [2,4–6]. Most of these techniques concentrate on the detection of water in honeycomb cells, while some focus on the detection of disbonds between the skin and core. However, none provide information regarding the state of the adhesive. Of all techniques currently available, few are well adapted to in situ detection of the problem.

Here, we report the results of an investigation into the feasibility of MRI as a nondestructive testing (NDT) technique for detecting water inside of composite sandwich panels well as degradation of the adhesive in these structures. Conventional magnetic resonance (MR) will clearly be sensitive to the presence of water. An additional potential advantage is that MR should also be sensitive to hydrogen found in the epoxy adhesive. Because of this, unlike other NDT techniques, the potential exists for the adhesive layer to be classified as 'normal' or 'degraded' through MR.

* Corresponding author. Fax: +1-506-453-4581.
E-mail address: bjb@unb.ca (B.J. Balcom).

1090-7807/$ - see front matter © 2004 Elsevier Inc. All rights reserved.
doi:10.1016/j.jmr.2004.02.011

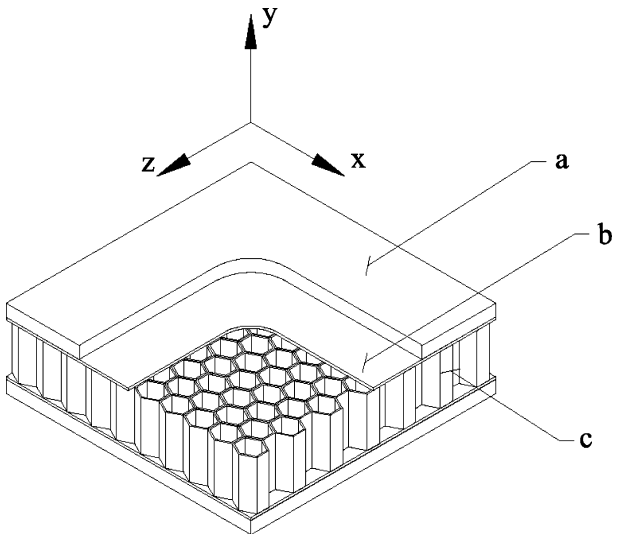

Fig. 1. Cut-away diagram showing the construction of aluminum/graphite-epoxy sandwich panels. The structure consists of a carbon fibre-epoxy composite skin (a), bonded to an aluminum honeycomb core (c) with epoxy (b). The hexagonal cells in the sample under study have a width of 4.75 mm (3/16") and a depth of 13 mm (1/2"). The aluminum foil was 50 μm thick. The graphite-epoxy composite layer was approximately 1 mm in thickness.

There are a number of challenges that must be addressed to make MR investigation of honeycomb-core sandwich panels viable. The presence of the aluminum honeycomb core, as well as the graphite fibres in the composite skin, cause difficulties in obtaining a signal from inside the core. The conductive materials in this structure can act as a shield, preventing the penetration of the radio frequency (RF) B_1 field. Eddy currents induced in these materials by B_1, as well as gradient switching can also introduce image artifacts [7]. Susceptibility differences inside of these heterogeneous structures also introduce inhomogeneities in the static B_0 field [8], shortening signal lifetimes, decreasing image resolution, and potentially causing further image distortion. Compounding these issues is the problem of obtaining MR information from a large sample such as an aircraft.

MRI is traditionally a laboratory technique as the size of the specimen is limited by the diameter of the bore of the magnet. This limitation may be overcome through the use of a unilateral, near surface MR sensor such as the NMR-MOUSE [9]. The ultimate application of the work presented here is the implementation of a MOUSE-like portable sensor for the in situ detection of anomalies in sandwich panels. Such a sensor could accomplish this through the detection of an MR signal from water inside of the honeycomb cells, or through the characterization of the signals obtained from the adhesive layer.

In this work, we examine the effects of the conductive materials within a small sandwich panel test sample on the MR signal obtained from a more conventional MRI experiment. We anticipate that knowledge gained through this MRI study will be transferable to future NMR-MOUSE investigations.

The single point imaging (SPI) family of pure phase encode MRI methods were the techniques of choice in this application due to their immunity to distortions in B_0 caused by sample inhomogeneity [10]. SPRITE [11], a variation of SPI employing ramped gradients, is particularly useful in imaging this type of sample as it permits the visualization of solid materials with short relaxation times. In SPRITE, k-space is sampled by varying the gradient values rather than the encoding time as in a frequency encoded image. Because of this, loss of signal due to T_2^* decay does not decrease image resolution. However, distortion of applied gradient fields in heterogeneous samples must be addressed as this could theoretically cause blurring. As will be shown, this distortion will not reduce image resolution but can potentially cause slight variations in local image intensity.

2. Theory

2.1. B_0 Distortion

The presence of a largely metallic structure in the volume being imaged will distort the homogeneities of both B_0 and any applied gradient fields due to the susceptibility difference between the metal and surrounding materials. The mean local field strength, B_0^s, in a material with magnetic susceptibility, χ_m, polarized in a magnetic field B_0 is given by

$$B_0^s = (1 + \chi_m)B_0. \tag{1}$$

In a heterogeneous sample, χ_m is not constant with position. Applying Maxwell's Equations to the magnetic field intensity vector, $\vec{H}_n$, and magnetic field strength vector, $\vec{B}_n$, at a boundary of two regions $(n = 1, 2)$ of differing susceptibility results in

$$\hat{n} \times (\vec{H}_2 - \vec{H}_1) = 0, \tag{2}$$

$$\hat{n} \bullet (\vec{B}_2 - \vec{B}_1) = 0, \tag{3}$$

where $\hat{n}$ is a vector normal to the boundary. Eq. (2) states that the tangential components of $\vec{H}$ must be continuous across the boundary. Eq. (3) states that the normal components of $\vec{B}$ must be continuous. These constraints introduce inhomogeneities in B_0 near susceptibility boundaries which may have a deleterious effect on image quality and resolution [12]. In linear media, the magnitude of the field inhomogeneity is proportional to the magnitude of the applied static field. Thus, the local magnetic field offset, ΔB_0 can be written as

$$\Delta B_0 = B_0(\Delta B_0'), \tag{4}$$

where $\Delta B_0'$ is a unitless measure of the inhomogeneity, often quoted in parts per million (ppm).

After excitation in a 1D MRI experiment at static field strength B_0, the phase, $\phi(t)$, of the resulting FID signal evolves according to

$$\phi(t) = \gamma t_p B_0 + \gamma t_p G_x x, \tag{5}$$

where G_x is the gradient applied in the x-direction, γ is the gyromagnetic ratio, and t_p is the encoding time. If the signal is demodulated, the contribution from B_0 is not seen and the resulting MR signal, in terms of the reciprocal space variable, $k_x = (2\pi)^{-1}\gamma G_x t_p$, becomes

$$S(k_x) = \int \rho(x) e^{-t_p/T_2} e^{j\phi(k_x)}\, dx = \int \rho(x) e^{-t_p/T_2} e^{j2\pi k_x x}\, dx, \tag{6}$$

which, neglecting T_2, the spin–spin relaxation time constant, is related to the proton density, $\rho(x)$, by Fourier transform.

If there are local static field offsets, represented by $\Delta B_0(x)$, the local phase of the signal will vary accordingly. With this variation included, Eq. (6) is written as

$$S(k_x) = \int \rho(x) e^{-t_p/T_2} e^{j\gamma \Delta B_0 t_p} e^{j2\pi k_x x}\, dx. \tag{7}$$

The effect of the additional term in this equation is a loss of signal due to the dephasing of spins across the sample. Note that $\Delta B_0(x)$ represents the magnitude of the magnetic field offset. The signal losses due to T_2 decay and B_0 inhomogeneity are traditionally combined to give the effective relaxation time

$$T_2^* = ((T_2)^{-1} + \gamma \Delta B_0)^{-1}. \tag{8}$$

The signal now becomes

$$S(k_x) = \int \rho(x) e^{-t_p/T_2^*} e^{j2\pi k_x x}\, dx. \tag{9}$$

While $\Delta B_0(x)$ represents the local offset of B_0, the value ΔB_0 used in the calculation of T_2^* is context specific as it quantifies the range of offsets across the volume from which signal is being measured. In the case of an image, it represents the distribution of B_0 offsets in one pixel.

If the encoding time is varied to encode position information in k-space, as is the case in frequency encoded images, the T_2^* decay in Eq. (9) causes the reconstructed image to be both blurred and distorted [12]. In phase-encode imaging, the encoding time remains constant and the gradient amplitudes are varied. Because of this, the effects of T_2^* decay on the signal are constant throughout k-space resulting in signal attenuation but no geometric distortion in the image.

2.2. Gradient distortion

When susceptibility inhomogeneities exist, *any* applied static magnetic field is distorted in the manner described by Eq. (4). This means that any applied gradient fields will also be distorted. This distortion will not be constant with position in k-space for a phase encoded image since the gradient strengths vary with k. Such a variation introduces the potential for blurring or geometric distortion of an acquired image. In one dimension, the gradient distortion at position, x, will be governed by the strength of the gradient field at that point, $G_x x$, and the inhomogeneity, $\Delta B_{0x}'(x)$, which relates a field applied in the x-direction to the resulting field offset in that direction. Therefore, the acquired signal in an MR experiment with only the terms related to this distortion included can be written as

$$S(k_x) = \int \rho(x) e^{j2\pi k_x x} e^{j\gamma G_x t_p x \Delta B_0'(x)}\, dx = \int \rho(x) e^{j2\pi k_x (x+g(x))}\, dx, \tag{10}$$

where $g(x) = x\Delta B_{0x}'(x)$ represents the susceptibility induced variations in k-space position. The quantity $g(x)$ has the unit of meters, and it can be observed from Eq. (10) that the proton density $\rho(x)$ is actually being encoded at position $x + g(x)$. Although theoretically this will lead to geometric distortions in the acquired image, by breaking down the exponential term in Eq. (10) using $e^{j\theta} = \cos\theta + j\sin\theta$ and assuming $g(x)$ is small to the point where $\cos(2\pi k_x g(x)) \approx 1$ and $\sin(2\pi k_x g(x)) \approx 2\pi k_x g(x)$, Eq. (10) becomes

$$S(k_x) \approx \int \rho(x) e^{j2\pi k_x x}\, dx + j2\pi k_x \int \rho(x) g(x) e^{j2\pi k_x x}\, dx. \tag{11}$$

Eq. (11) shows that for small local variations of the applied gradient field, the Fourier transform of the acquired signal results in a spatial map of proton density suffering from no geometric distortion but from a spatially dependent error term, $\xi(x)$:

$$\rho(x) \approx \mathbf{F}\{S(k_x)\} - \xi(x), \tag{12}$$

where

$$\xi(x) = \mathbf{F}\{j2\pi k_x \int \rho(x) g(x) e^{j2\pi k_x x}\, dx\} \tag{13}$$

and $\mathbf{F}\{\}$ represents the Fourier transform.

Equations (12) and (13) describe the error due to gradient distortion for the 1D case and cannot be directly applied to two dimensions. For the 2D and 3D cases, we must consider the effects of the gradient field in a given direction on the resulting magnetic fields in the other direction(s). For example, in two dimensions, a field applied in the x-direction will result in a field component in the y-direction. This behaviour can be described by

$$B_{Gx}(x,y) = G_x x + G_x x \Delta B_{0xx}'(x,y) + G_y y \Delta B_{0xy}'(x,y) \tag{14}$$

and

$$B_{Gy}(x,y) = G_y y + G_x x \Delta B'_{0yx}(x,y) + G_y y \Delta B'_{0yy}(x,y). \quad (15)$$

Here, $B_{Gx}(x,y)$ and $B_{Gy}(x,y)$ are the x- and y-direction components of the magnetic field at position (x,y) due to the applied gradients G_x and G_y. The function $\Delta B'_{0xy}(x,y)$ represents the ratio of the field offset in the x-direction to the applied field in the y-direction causing this offset. Using the reasoning that led to Eq. (13), the 2D local image error, $\xi(x,y)$, can be written as

$$\xi(x,y) = \mathbf{F}\left\{ \int\int \mathrm{j}2\pi\rho(x,y)(k_x g_x(x,y) + k_y g_y(x,y))\mathrm{e}^{\mathrm{j}2\pi(k_x x + k_y y)}\,\mathrm{d}x\,\mathrm{d}y \right\}. \quad (16)$$

In this case,

$$g_x(x,y) = x(\Delta B'_{0xx}(x,y) + \Delta B'_{0yx}(x,y))$$

and

$$g_y(x,y) = y(\Delta B'_{0xy}(x,y) + \Delta B'_{0yy}(x,y)).$$

The net result of this error is small variations in the local image intensity. As will be seen in Section 3.1, the magnitude of this error is negligible in most practical situations and therefore does not prevent high resolution images from being obtained in the presence of sample inhomogeneities if phase encoding is employed.

2.3. B_1 attenuation

When conductors are present in or around the sample being investigated, attenuation of the RF B_1 field can often become a severe impediment to signal acquisition. Conductors are generally characterized as having a skin depth, the distance to which a RF field will penetrate at a given frequency. Since the eddy currents resulting from Faraday's Law are proportional to the rate of change of B_1, skin depth decreases with increasing frequency.

A B_1 field whose strength varies through the sample will introduce intensity errors in an image because the flip angle will vary across the sample. While no blurring of acquired data will take place as a result of B_1 distortions, the flip angle through which the magnetization of the sample is rotated after excitation will vary spatially, resulting in an observed proton density that varies accordingly [7]. Furthermore, the principle of reciprocity [13] states that the B_1 distribution is proportional to the local sensitivity of the coil used in an experiment and thus the signal obtained from regions of space where B_1 is higher will be correspondingly higher.

3. Results/discussion

The sample under study was a 4 cm square section of aluminum honeycomb sandwich panel of the type illustrated in Fig. 1. The honeycomb core was 13 mm in thickness and each cell was 4.75 mm in width. The adhesive used in this sample was Cytec FM-300 epoxy, an industry standard bonding agent for this type of application. Ten of the central cells of this sample were each partially filled with 100 μL of water via small holes drilled through the composite skin which were then sealed.

3.1. B_0 distortion simulations

The B_0 distortions due to susceptibility inhomogeneities in the sample were simulated using the commercial Finite Element simulation software, FEMLAB. The simulation consisted of a 2 D (XZ plane in Fig. 1) cross section of aluminum honeycomb with ten central cells filled with water. It was anticipated that the presence of the aluminum in the structure would cause inhomogeneities in B_0. A contour plot of the simulated magnetic field distortion, $\Delta B'_0$, in parts per million, is reproduced as Fig. 2. From this plot, we observe that the magnetic field in the centre of the water filled section experiences relatively little distortion while the field inhomogeneity is much higher at the interface between the outer cells and the surrounding area. This would indicate that the aluminum inside of the structure has an effect on B_0 homogeneity that is minor compared to the effects of the susceptibility difference between the water and surrounding air. In order to confirm this, the simulation was repeated with the aluminum removed but the geometry of the water in the cells left intact. Fig. 3 shows the distribution of $\Delta B'_0$, simulated for the case where the aluminum was included as well as the case where it was

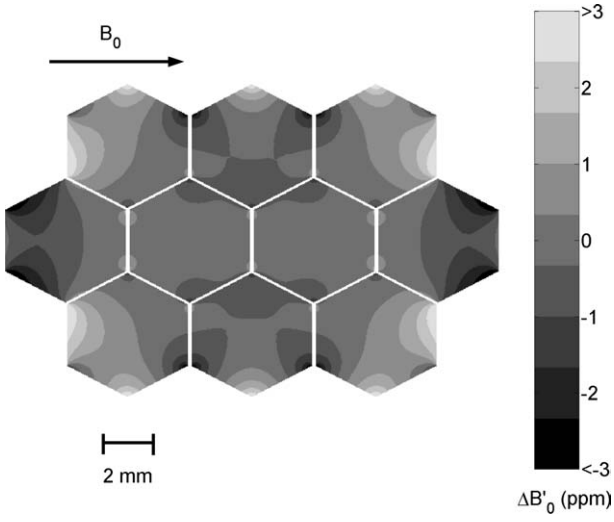

Fig. 2. Plot showing the simulated $\Delta B'_0$ distortion due to the shape of the water containing cells. The simulation geometry consisted of 10 water filled cells in an aluminum honeycomb lattice. It is observed that the maximum distortion occurs at the interface between the exterior cells and surrounding air but little distortion occurs in the interior of the cluster of filled cells.

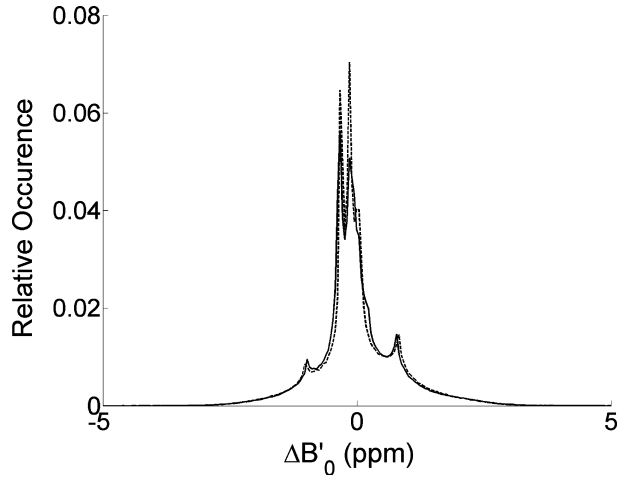

Fig. 3. Plot showing the simulated B_0 inhomogeneity ($\Delta B_0'$) distribution due to the geometry of the water inside of the aluminum honeycomb. The solid line corresponds to the simulation that included the effects on B_0 of the air, aluminum, and water, while the dashed line represents the effects of the air and water only. Comparing the two curves reveals that the presence of the aluminum makes little difference regarding the homogeneity of B_0, which is governed primarily by the susceptibility difference between water and air.

excluded. The similarities between the two results confirm that the aluminum lattice has a very small effect on the homogeneity of B_0 in the sample, although the field is nevertheless distorted due to the geometry of the water and the susceptibility difference between it and the surrounding air.

From the distribution of B_0 offsets simulated, a bulk T_2^* value was calculated by simulating the signal loss due to dephasing of signals from individual pixels in the sample. The decaying signal was approximated as

$$s(t) = \sum_i \rho_{0i} e^{j2\pi\gamma\Delta B_{0i} t}, \tag{17}$$

were ρ_{0i} is the local proton density (assumed to be constant where water was present and zero elsewhere), and ΔB_{0i} is the local field offset.

Since the decays were not exponential, T_2^* was defined as the time in which the signal decayed to e^{-1} of its maximum value. For the cases of the aluminum and water as well as the water alone, T_2^* was calculated to be approximately 4.2 ms, with T_2 assumed to be long.

3.2. Gradient distortion simulations

The magnetic field inhomogeneity introduced by one hexagonal cell filled with water was simulated in the XZ plane. Using this data, the resulting error, $\xi(x,z)$, due to the distortion of gradient fields applied to this geometry was calculated. In order to examine the effects of a large distortion on image quality, the simulated field inhomogeneity was increased by a factor of one hundred. The resulting $g_y(x,z)$ map is reproduced as Fig. 4A as an example distortion function for this simulation. Its magnitude approaches 4 μm in places or 0.02% of the 2 cm × 2 cm field of view. This plot also shows the geometry of the simulation. Fig. 4B shows the error term, $\xi(x,z)$ which was calculated for the simulated B_0 distributions and the proton density illustrated in plot C of Fig. 4 using the approximation,

$$\xi(k_x,k_z) = \sum_p \sum_q j2\pi\rho(x_p,z_q)(k_x g_x(x_p,z_q) + k_z g_z(x_p,z_q))e^{j2\pi(k_x x_p + k_z z_q)} \tag{18}$$

derived from Eq. (16).

The reconstructed image is shown in plot D. The local intensity error is never more than 0.5%, and there is no geometric distortion. It was found that the approximation of the error, Eq. (16), held for this example even when the inhomogeneity was increased by a factor of 1000. Note that this error will be independent of the field of view: as the field of view narrows, the gradients increase, however the range of the spatial variables (x,z) decreases, causing g_x, g_z to remain the same. In a practical situation, this implies that image acquisition would be limited by signal loss due to a short T_2^* well before the error introduced by distorted gradients became a significant factor.

3.3. MR measurements

For pure water inside of the sandwich panel sample, the observed T_2^* was found to be on the order of 200 μs while a CPMG measurement revealed that the sample had a bulk T_2 of over 1 s. The measured T_2^* value is substantially lower than that predicted by the B_0 simulations but can be explained by the fact that the simulations were performed in two dimensions only and that they did not account for the presence of the graphite. Graphite is strongly paramagnetic and therefore would cause far more distortion in B_0 than water or aluminum.

MRI measurements of water within a sample of aluminum honeycomb without a composite skin were performed in order to confirm that the graphite skin was principally responsible for the short T_2^* values observed. A small section of aluminum honeycomb similar in size to the control surface test sample was imaged with a Gadolinium Chloride doped gel occupying a central cluster of cells. One cell was filled with the gel while several others were partially filled. The bulk T_2^* for this sample was found to be approximately 2.2 ms, within a factor of 2 of the simulated value. From this, we conclude that the presence of the graphite, and the resulting B_0 distortion, is the source of the short T_2^* observed in the sandwich panel sample. This value is an order of magnitude smaller than the measured and simulated T_2^* values for the sample without the composite skin.

By imaging the aluminum honeycomb (no composite skin) sample in two dimensions and observing local

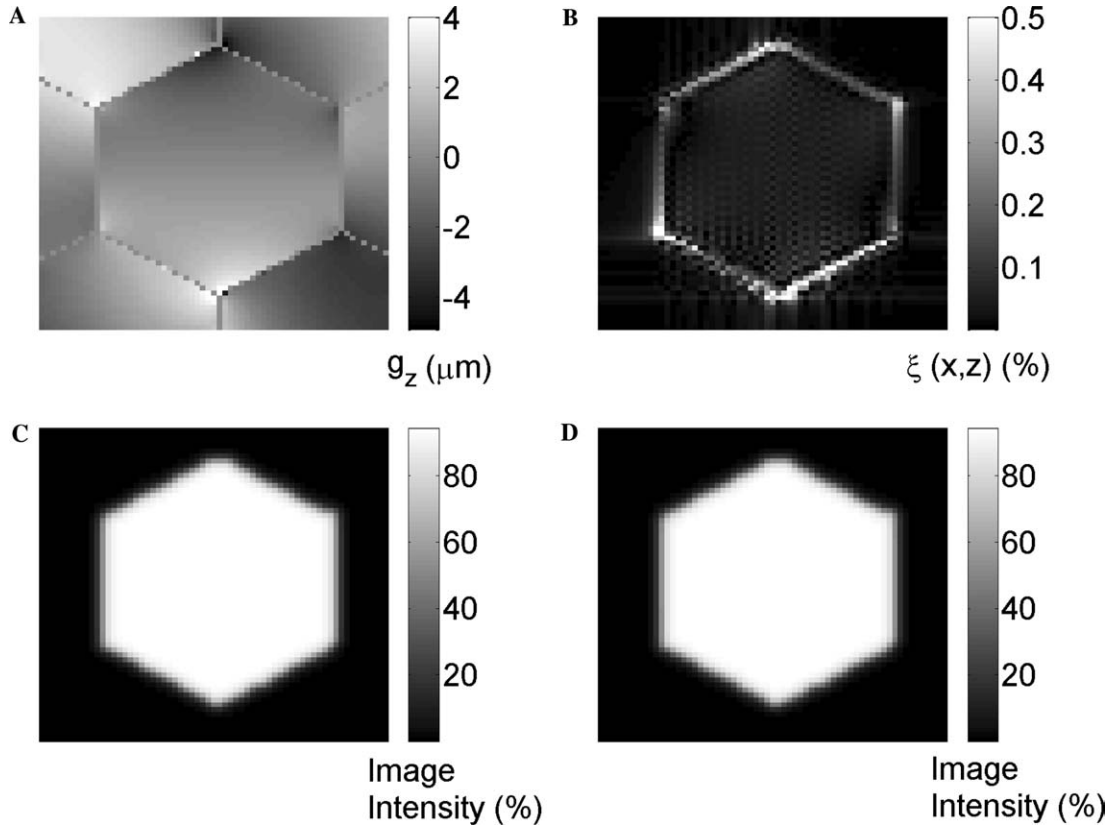

Fig. 4. Results of a numerical calculation of the image effects due to distorted gradients in the *XZ* plane when imaging one hexagonal cell filled with water inside of an aluminum honeycomb lattice. Plot (A) shows an example susceptibility induced distortion function, $g_z(x,z)$, for the extreme case of 100 times the distortion due to a single cell filled with water. Plot (B) shows the simulated error term $\xi(x,z)$. Plots (C,D), respectively, represent the image that would result for the cases of no gradient distortion and distortion effects included. Variations in the intensity of plot (D) are too small to discern, and there is no geometric distortion.

image intensity variations as a function of encoding time, it was possible to resolve local T_2^* values at different regions within the sample. Using this technique, T_2^* values below 500 μs were observed in pixels at the interface between air and water containing cells. Inside of water containing cells and at the boundaries of adjacent cells of this type, T_2^* was typically upward of 4000 μs and showed little variation near the boundaries.

3.4. B_1 attenuation simulations

A section of aluminum honeycomb sandwich panel was modelled using a 3D electromagnetic finite integration technique [14] based simulation software package (Microwave Studio) and the effects of this structure on a penetrating RF magnetic field were simulated. The field distribution inside of the structure resulting from RF excitation by a 1.2 cm diameter surface coil was obtained. This type of coil was chosen for the following reasons: (1) A single turn coil was simple to construct using the simulation tool. (2) Verification of the simulation results for the coil alone was possible since the magnetic field distribution due to a loop of current is well known. (3) This type of coil is characteristic of the type that would be used in a practical imaging application, for example, the NMR-MOUSE. (4) A similar surface coil is easy to construct, facilitating experimental verification.

The simulation geometry consisted of a cluster of cells with a composite skin as illustrated in Fig. 5. The simulated RF coil is also visible in this image. The aluminum lattice was modelled as a discrete heterogeneous structure in this simulation. Honeycomb cores are manufactured by gluing together successive ribbons of aluminum foil [15]. As a result, there is a gap on the order of 25 μm between neighboring ribbons in one direction while the metal is continuous in the other. Note that magnetic field penetration was only simulated for the case where B_1 was aligned parallel to the *y*-axis in Fig. 1 in the honeycomb structure. Fields oriented in other directions were not considered as they would encounter numerous layers of aluminum in this orientation and be rapidly attenuated.

Fig. 6 shows the simulated magnetic field strength (B_1) along the *y*-axis of the sample due to an RF current flowing through the coil. This plot presents the normalized field intensity on the axis of the coil for both 8 and 100 MHz as well as for the case of the coil radiating

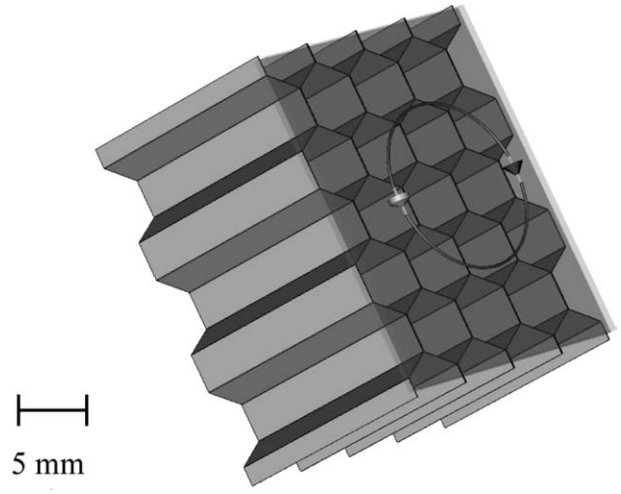

Fig. 5. Pictorial view of the aluminum/graphite-epoxy sandwich structure simulated using CST Microwave Studio. The 1.2 cm surface coil was positioned 1.5 mm above the structure which consisted of a 16 mm thick section of aluminum honeycomb clad in a skin comprised of conductive and dielectric layers.

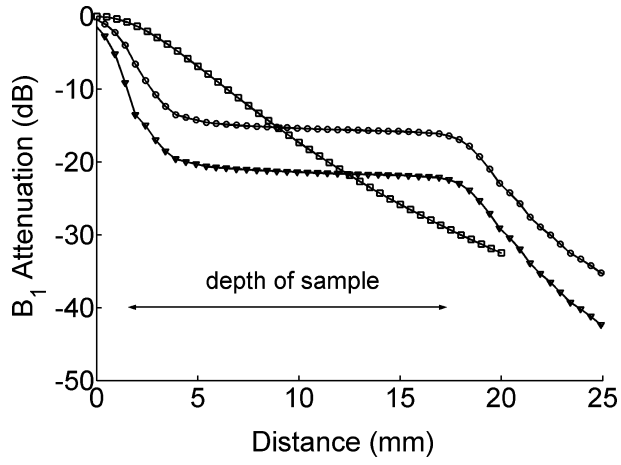

Fig. 6. Simulated magnetic field strength (B_1) on the axis of a 1.2 cm surface coil. Intensity profiles are shown for the case of a coil radiating into free space (□), and for the coil positioned 1.5 mm above a section of sandwich panel (B_1 penetrating into the structure in the y-direction) at 8 MHz (○) and 100 MHz (▽).

into free space. Only the component of this field perpendicular to the plane of the coil (y-component) is considered in this case.

This simulation shows that although the field strength drops sharply through the exterior of the panel, it remains relatively uniform throughout the honeycomb structure, eventually becoming stronger than the field due to the coil in free space. As predicted by skin depth theory, the attenuation of B_1 is frequency dependent; the higher frequency field experiences increased attenuation compared to the lower frequency field.

3.5. B_1 attenuation experiments

The simulated attenuation of B_1 was examined experimentally using a 'pickup coil' at 8.3 and 100 MHz and through imaging techniques at 8.3 MHz. A section of the graphite-epoxy composite was removed from a sample of sandwich panel so that a small (2 mm diameter) coil of wire could be placed inside of one of the cells. The sample was placed on a 1 cm surface coil and the voltage induced in the coil was recorded as its position was varied through the cell. The measured voltage is a direct measure of the strength of B_1 through Faraday's law. The results for 8.3 and 100 MHz, normalized by control measurements made on the coil at those frequencies without the sample present, are reproduced in Fig. 7. Although the field falls off slightly earlier than predicted by simulations, the results agree very well with those in Fig. 6. Because the entire extent of the sample was not accessible to the pickup coil, the measurements in Fig. 7 begin at approximately 5 mm from the surface coil, in the centre of the sample. Nevertheless, the latter portion of the plateau is still clearly visible.

The behaviour of B_1 inside of the honeycomb sandwich panel structure was investigated using SPI imaging at 8.3 MHz. Fig. 8A shows a 1D y-direction profile obtained from a phantom sample of doped water. This plot shows the sensitivity of the 1 cm surface coil used. The rapid decay in intensity with distance from the coil is expected in this situation as surface coils typically are only sensitive to a distance equal to their radius [16]. Fig. 8B shows the profile obtained from water inside of the aluminum structure. For this image, approximately

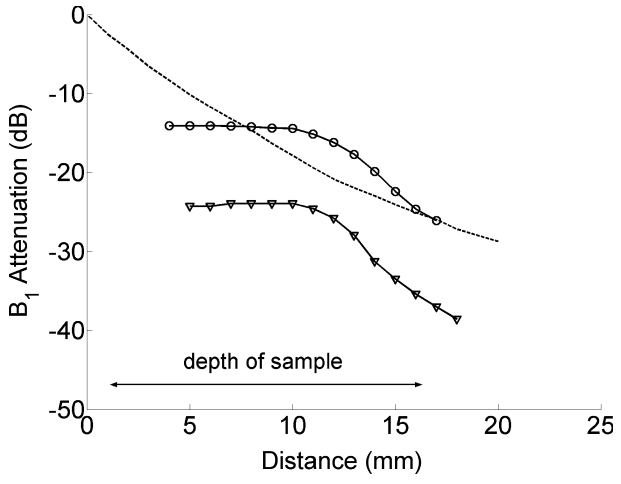

Fig. 7. Measured B_1 intensity inside of a single honeycomb cell along the y-direction in the composite test sample centred over a 1.0 cm surface coil at 8.3 MHz (○) and 100 MHz (▽). The arrows indicate the span of the sample. Note that no signal was obtained from the area closest to the surface coil since access to this area was blocked by the sample skin. The dashed line represents the measured field strength due to the coil without the sample present.

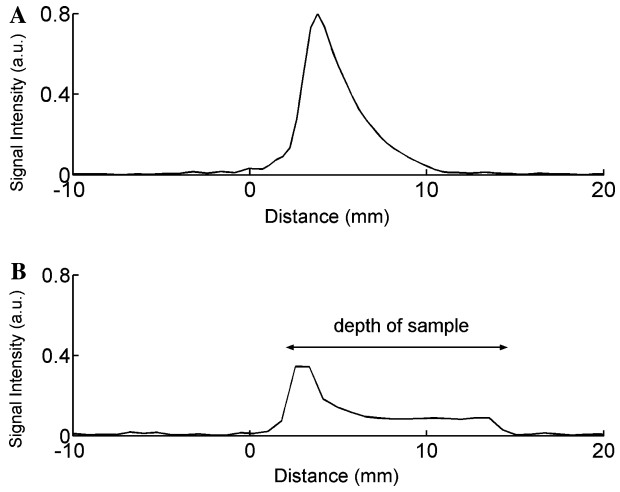

Fig. 8. One dimensional y-direction profiles (averaged over the X and Z directions) of the signal intensities obtained from a phantom sample (A) and water inside of a test sample of sandwich panel (B). These acquisitions were performed at 8.3 MHz. The test sample in this case had approximately ten of its central cells completely filled with water. In both cases, the samples were placed directly adjacent to a 1.0 cm surface coil and the field of view in each case is the same. Plot (A) simply shows the sensitivity of the surface coil while (B) shows how this sensitivity has changed due to the presence of the sandwich panel. Note that although the signal in (B) is attenuated compared to (A), the signal intensity does not decay with distance from the coil in the same manner but rather, after an initial attenuation, becomes constant throughout the remainder of the sample. The signal in (B) only decays when the end of the sample has been reached.

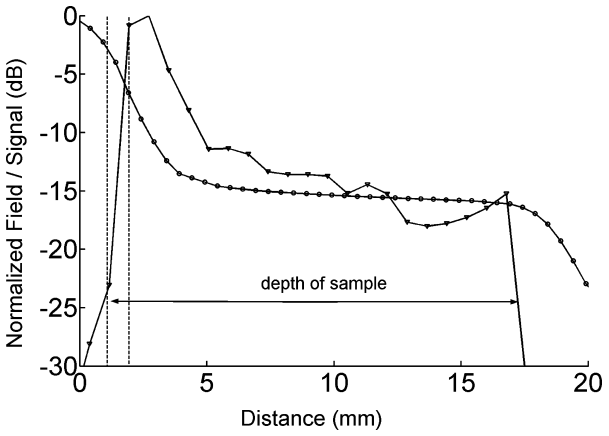

Fig. 9. Comparison of the observed signal (▽) and simulated magnetic field strength (○) inside of a sandwich panel structure due to a surface coil resonating at 8.3 MHz (B_1 penetrating into the sample in the Y-direction). The plane of the surface coil is located at position 0 on the distance axis. The region between the dotted lines represents the graphite skin.

10 cells in the centre of the structure were filled with water doped with Gadolinium Chloride. Although the signal from the water inside of the structure experiences a sharp initial attenuation, the maximum distance at which the surface coil is able to acquire a signal is increased due to an apparent 'guiding' effect from the aluminum channels. The signal in this case vanishes only at the opposite side of the sample. From the principle of reciprocity, the signal intensity observed in an image can be used to approximate the B_1 distribution. Furthermore, in areas where B_1 is weaker, a correspondingly lower flip angle will be achieved, resulting in less signal. The 'plateau' in image intensity observed in Fig. 8B therefore indicates that both the sensitivity of the coil, and the flip angle, remain relatively constant along the y-axis through the centre of the sample. Fig. 9 shows the normalized simulated B_1 field distribution through the sandwich panel structure directly below a surface coil overlaid with the B_1 field distribution derived from this imaging experiment. The excellent agreement between these two curves reinforces the validity of the simulation model.

Figs. 6–9, characterize the behaviour of B_1 inside of the sandwich panel sample. Note that the graphite-epoxy skin is responsible for the majority of the attenuation in B_1. Fig. 9 indicates the 'skin' region and shows a steep drop in B_1 as is passes through the skin. With this transition complete, attenuation inside the cells settles to a small value. Simulations of longer cells have confirmed that B_1 continues to fall off in this manner regardless of the cell length. Measurements made on aluminum honeycomb alone confirm that there is little difficulty in imaging water inside of their cells, even at 100 MHz where skin depth becomes more of a concern. In samples covered in graphite-epoxy skin, however, imaging of water in the centre of the sample proved much more challenging. As with the distortion of B_0, it is primarily the graphite skin that makes this a challenging sample.

3.6. 3D Imaging

With appropriate imaging parameters employed, it was possible to obtain more detailed images of the structure at 100 MHz. The SPRITE technique is best suited to imaging materials with short relaxation times and, using this method, it proved possible to obtain a signal not only from the water inside of the sample but also from the adhesive bonding the composite skin to the aluminum.

Fig. 10 shows 3D rendered images of the sample acquired at 100 MHz. In this case, a small amount of water was present in the central cells of the sample as can be clearly observed in these images. For this acquisition, the encoding time was short enough that signal from the adhesive was also captured. The T_2^* of the FM-300 adhesive was less than 150 μs. The image was acquired with conservative timing parameters in an overnight experiment.

Fig. 11 shows a slice in the XZ plane extracted from the 3D data set. This image represents the sample's measured spin density averaged over a slice

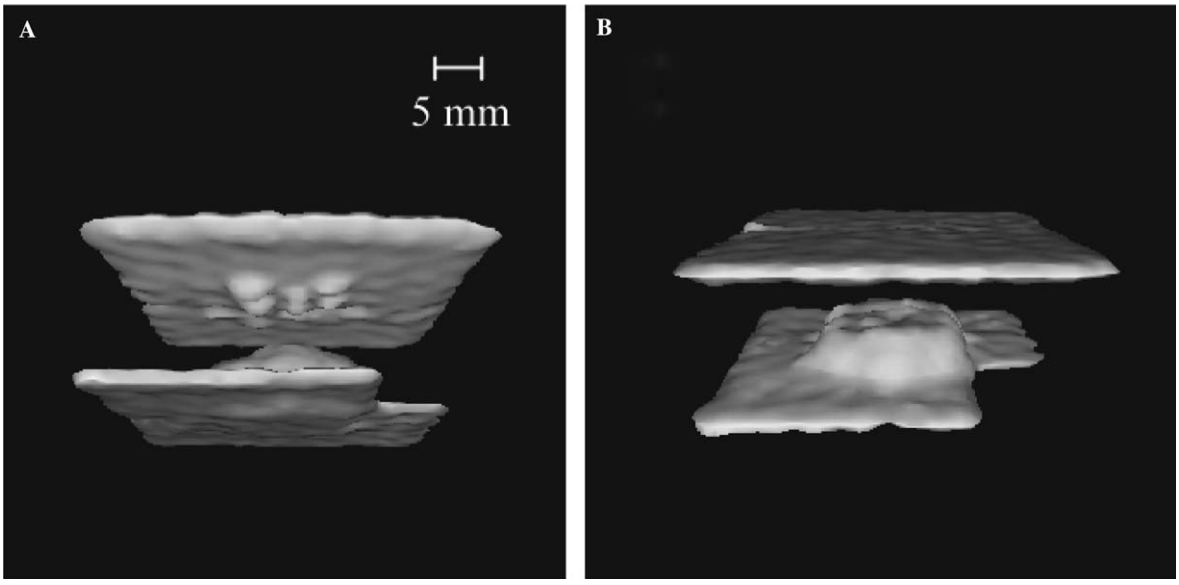

Fig. 10. Three dimensional rendered SPRITE image of the composite sandwich panel test sample. Signal from both the water and the epoxy/adhesive layer is apparent. The nominal resolution is 0.9 mm. Ten central cells in the test sample were partially filled with 100 μL of pure water for this image. Water partially filling the bottom of these cells is present (B), along with small, pendant drops on the top surface of some cells (A). Adhesive was removed from one corner of the structure resulting in the area of 'missing' signal in the bottom right corner of both images.

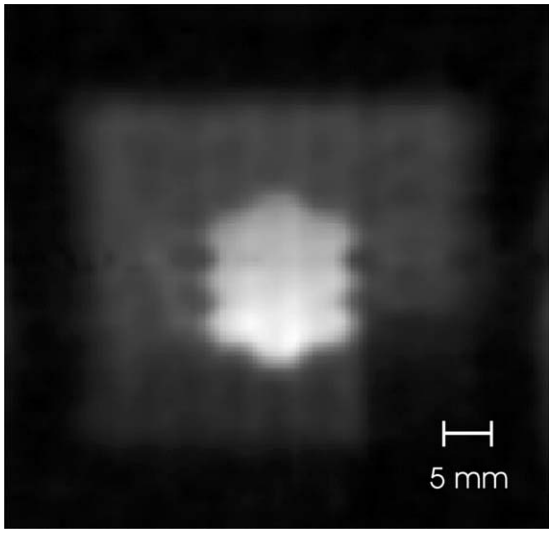

Fig. 11. Slice extracted from a 3D SPRITE image of the composite sandwich panel test sample. This slice corresponds to a section approximately 0.9 mm thick in the X–Z plane spanning the adhesive and aluminum honeycomb regions. The nominal transverse resolution is also 0.9 mm. The bright central region in the image corresponds to the region of central cells that were partially filled with water. Note that although this water is surrounded by the heterogeneous structure of the sandwich panel, no geometric distortion has taken place in this image. This is clear as the hexagonal pattern of the aluminum cells can be seen both around the edges of the water bearing cells and as a regular pattern throughout the image of the surrounding composite. The area of 'missing' signal in the bottom right corner indicates where the adhesive was removed.

approximately 0.9 mm in thickness. In this image, signal from water in the central cells is clearly visible, as is signal from the adhesive. The sample imaged in this case had a thin portion of the adhesive removed from one of its corners. This can be seen as an absence of signal from the bottom right corner of the image. In this slice, it is possible to see the hexagonal cell shape both around the periphery of the water bearing cells as well as in the regular pattern visible in the portion of the image where no water was present as this slice spans the aluminum, adhesive, and skin regions. The source of this pattern is the adhesive fillets bonding the skin to the aluminum honeycomb. The adhesive thickness is not constant across the interface between each cell and the skin. Rather, it 'rides up' the aluminum, forming a meniscus in each cell.

4. Conclusions

Distortion-free imaging of water inside of a conductive structure, representative of a control surface in a modern, high performance aircraft, has been demonstrated. Although the B_1 field is attenuated at both 8 and 100 MHz, visualization of water near the surface of the sandwich panel, as well as signal from the adhesive present in this structure is possible using the SPRITE technique. Despite inhomogeneities in the B_0, and gradient fields, due to the heterogeneous nature of the sample, the SPRITE images are distortionless to the point where even the subtle variation in the signal from the adhesive due to bonds with the aluminum can be visualized.

Given these results, characterization of the MR signals from a sample that has suffered from adhesive

degradation should prove straightforward in laboratory research applications. Challenges lie in applying measurement techniques to field applications due to the inhomogeneous nature of the static field produced by a single sided NMR device. However, a MOUSE-like instrument may be a viable approach for field non-destructive testing of aircraft.

5. Experimental

B_0 distortions, in the presence of the aluminum honeycomb, were simulated using the commercial FEMLAB 2.3 (Comsol, Burlington, MA) finite element simulation software package. The validity of the results were verified by simulating the magnetic field inhomogeneities introduced by geometries for which analytical solutions exist. Excellent agreement was found between FEMLAB results and theory for the case of a cylinder and an annular cylinder. The susceptibility values used in the simulations were $\chi = 2.07 \times 10^{-5}$ for aluminum, 9.0×10^{-6} for water, and 3.6×10^{-7} for air. The effects of the composite skin were not included. A square lattice of 22 honeycomb cells was simulated with ten cells in the centre filled with water. The simulation used 174,312 triangular finite elements.

RF simulations employed the Microwave Studio 4.0 (Computer Simulation Technology, Darmstadt, Germany) Finite Integration Technique based software package. The structure was modelled as a series of adjacent ribbons of corrugated aluminum forming a honeycomb lattice of the type seen in Figs. 1 and 5. The graphite-epoxy skin was modelled as a thin (50 μm) sheet of graphite (conductivity, $\sigma = 7 \times 10^4\,(\Omega\mathrm{m})^{-1}$) between two 0.5 mm layers of dielectric ($\varepsilon_r = 3$). This model was found to agree with measured data. The simulation used 227,994 mesh cells to model a 40 mm × 40 mm × 40 mm region containing the geometry seen in Fig. 5. The dimensions of the simulated cells were the same as those in the test sample.

MR experiments were performed on test samples characteristic of the honeycomb sandwich panels being studied. These panels, prepared by Captain Sylvain Giguère of AVRS DND, were approximately 4 cm square and 13 mm thick, with cells 4.75 mm in width, of the construction illustrated in Fig. 1. The graphite-epoxy skin was 1 mm thick and bonded to the aluminum honeycomb using Cytec FM-300 epoxy. Small holes were drilled in one face of the sample in order to place 100 μL of water in each of ten cells in the centre of the sample. For experiments at 0.2 T, the water injected inside of the sample was doped with Gadolinium Chloride to a concentration of 0.4 mmol. The aluminum honeycomb sample imaged at 2.4 T had its cells filled with a gel made of Gadolinium Chloride doped water and agar.

Imaging at 8.3 MHz was performed using a 0.2 T permanent magnet with a 14 cm pole gap, employing a home-built gradient system driven by Techron (Elkhart, IN) 7700 gradient amplifiers. A home-built nominal 1 cm (exterior diameter, 1.2 cm) diameter multi-turn surface coil powered by a 300 W AMT (Brea, CA) 3205 RF amplifier was used for excitation and detection. The acquisition was controlled by a Tecmag (Houston, TX) Apollo console. All images at this frequency used the SPI imaging technique.

Experiments at 100 MHz used a Nalorac (Matrinez, CA) 2.4 T 32 cm horizontal bore superconducting magnet with a Nalorac 7.5 cm i.d. water cooled gradient system (max gradient 100 Gauss/cm) driven by Techron 8710 gradient amplifiers. Imaging of the composite sandwich panel employed a home-built, 32-strut, 20 cm long, 4.5 cm i.d. birdcage resonator. Aluminum honeycomb (no skin) sample measurements employed a homemade 4.0 cm diameter surface coil. Both probes were powered by a 2 kW AMT 3445 RF amplifier. Acquisitions were controlled by a Tecmag Libra console. All experiments were performed at ambient temperature. All images with this system employed the SPRITE imaging modality.

The 3D SPRITE image was acquired with a 6 cm × 6 cm × 6 cm field of view using $64 \times 64 \times 64$ points and 64 averages. The pulse length was 5 μs (the nominal 90° pulse measured for the sample was about 30 μs), with a repetition time of 2 ms. The encoding time was 80 μs. The maximum gradient was 16 Gauss/cm.

1D profiles were acquired using SPI with a 5 cm field of view, 64 points and 64 averages. The sandwich panel measurements used 80 μs pulses, an encoding time of 1 ms and a last delay of 200 ms. There was no nominal 90° pulse for this sample as B_1 was inhomogeneous as a result of both the attenuation effects from the sample and the surface coil used. The reported pulse width was selected to maximize the signal-to-noise in the image. The maximum gradient was 1.5 Gauss/cm.

Acknowledgments

We thank the Canadian Department of National Defence for sample materials and funding. We also thank Ken McRae and Captain Sylvain Giguère from AVRS DND for their expert advice. B.J.B. thanks NSERC of Canada for equipment and operating grants. I.V.M. thanks NSERC of Canada for an operating grant. A.E.M. thanks NSERC of Canada (USRA) and the New Brunswick Innovation Foundation for research funding. G.L. thanks NSERC of Canada for a Post Graduate Scholarship. The UNB MRI Centre is supported by an NSERC Major Facilities Access Award. B.J.B. is the holder of a Canada Research Chair.

References

[1] K.F. Karlsson, B.T. Aström, Manufacturing and applications of structural sandwich components, Composites Part A: Applied Science and Manufacturing 28 (2) (1997) 97–111.
[2] J.S.R. Giguère, Damage mechanisms and nondestructive testing in the case of water ingress in CF-18 flight control surfaces, Tech. rep., Defence and Civil Institute of Environmental Medicine, DCIEM TM 2000-098 (August 2000).
[3] T.C. Radtke, A. Charon, R. Vodicka, Hot/wet environmental degredation of honeycomb sandwich structure representative of F/A-18: flatwise tension strength, Tech. rep., Defence Science and Technology Organization: Aeronautical and Maritime Research Laboratory, DSTO-TN-0908 (1999).
[4] R.A. Pethrick, D. Hayward, Investigation of dielectric methods for the characterization of adhesive bonded structures, Tech. rep., AFRL-SR-BL-TR-01-0561 (September 2000).
[5] G.D. Davis, L.A. Krebs, C.M. Dacres, Sensor to detect moisture/degradation of composite and adhesive bonds, in: Proceedings of the International SAMPE Symposium and Exhibition, vol. 46, 2001, pp. 20–29.
[6] A. Charon, Hot/wet environmental degradation of honeycomb sandwich structure representative of F/A-18: discoloration of Cytec FM-300 adhesive, Tech. rep., Defence Science and Technology Organization: Aeronautical and Maritime Research Laboratory, DSTO-TN-0263 (2000).
[7] L.W. Bartels, C.J. Bakker, M.A. Viergever, Improved lumen visualization in metallic vascular implants by reducing RF artifacts, Magn. Res. Med. 46 (2002) 171–180.
[8] P.T. Callaghan, L.C. Forde, C.J. Rofe, Correlated susceptibility and diffusion effects in NMR microscopy using both phase-frequency encoding and phase-phase encoding, J. Magn. Res. B 104 (1994) 34–52.
[9] G. Eidmann, R. Savelsberg, P. Blümler, B. Blümich, The NMR MOUSE, a mobile universal surface explorer, J. Magn. Res. A 122 (1996) 104–109.
[10] S. Gravina, D.G. Cory, Sensitivity and resolution of constant-time imaging, J. Magn. Res. 104 (1994) 53–61.
[11] B.J. Balcom, R.P. MacGregor, S.D. Beyea, D.P. Green, R.L. Armstrong, T.W. Bremner, Single point ramped imaging with T_1 enhancement (SPRITE), J. Magn. Res. B 123 (1996) 131–134.
[12] P.T. Callaghan, Principles of Nuclear Magnetic Resonance Microscopy, Clarendon Press, New York, 1991.
[13] H. Vesselle, R. Collin, The signal-to-noise ratio of nuclear magnetic resonance surface coils and application to a lossy dielectric model-part I: theory, IEEE Trans. Biomed. Imag. 42 (5) (1995) 497–506.
[14] M. Dehler, T. Weiland, Status and future of the 3D MAFIA group of codes, IEEE Trans. Magn. 26 (2) (1998) 751–754.
[15] S.K. Mazumdar, Composite Manufacturing: Materials, Product, and Process Engineering, CRC Press, Boca Raton, FL, 2001.
[16] B.H. Suits, A.N. Garroway, J.B. Miller, Surface and gradiometer coils near a conducting body: The liftoff effect, J. Magn. Res. 135 (1998) 373–379.